

The impact of macroscopic epistasis on long-term evolutionary dynamics

Benjamin H. Good¹ and Michael M. Desai¹

¹*Department of Organismic and Evolutionary Biology, Department of Physics, and FAS Center for Systems Biology, Harvard University, Cambridge MA 02138*

Genetic interactions can strongly influence the fitness effects of individual mutations, yet the impact of these epistatic interactions on evolutionary dynamics remains poorly understood. Here we investigate the evolutionary role of epistasis over 50,000 generations in a well-studied laboratory evolution experiment in *E. coli*. The extensive duration of this experiment provides a unique window into the effects of epistasis during long-term adaptation to a constant environment. Guided by analytical results in the weak-mutation limit, we develop a computational framework to assess the compatibility of a given epistatic model with the observed patterns of fitness gain and mutation accumulation through time. We find that the average fitness trajectory alone provides little power to distinguish between competing models, including those that lack any direct epistatic interactions between mutations. However, when combined with the mutation trajectory, these observables place strong constraints on the set of possible models of epistasis, ruling out most existing explanations of the data. Instead, we find the strongest support for a “two-epoch” model of adaptation, in which an initial burst of diminishing returns epistasis is followed by a steady accumulation of mutations under a constant distribution of fitness effects. Our results highlight the need for additional DNA sequencing of these populations, as well as for more sophisticated models of epistasis that are compatible with all of the experimental data.

A central feature of evolutionary adaptation is that the space of potential innovations can vary with the evolutionary history of a population. Examples are common in the microbial world: the ability to import a nutrient may be beneficial only if a mechanism has evolved to utilize it (Quandt et al., 2014), while a previously advantageous drug resistance mutation can be rendered obsolete by the acquisition of a second resistance allele (Weinreich et al., 2006). This capacity for evolutionary feedback is quantified in terms of *epistasis*, which measures how the effect of a mutation depends on the genetic background in which it arises. In principle, epistasis can lead to widespread historical contingency, and can fundamentally alter the dynamics of adaptation (Wright, 1932; Gould, 1989). But in practice, the long-term evolutionary impact of epistasis remains largely uncharacterized.

Empirical patterns of epistasis are most commonly measured using a direct approach (see (de Visser and Krug, 2014) for a recent review). Candidate mutations are introduced into a set of genetic backgrounds via crossing or other genetic reconstruction techniques, and the fitnesses of the reconstructed genotypes are measured using competitive fitness assays or related proxies. These data yield a functional relationship between the fitness effect of a mutation and its genetic background, with the traditional pairwise epistasis emerging as a special case when the backgrounds are single mutants. We will use the term *microscopic epistasis* to refer to these measurements, since they track the background-dependence of individual mutations. Of course, the precise background dependence of any given mutation is essentially an empirical matter: the fitness effects depend on the biological details of the organism, its environment, and the iden-

ties of the mutations themselves. Empirical estimates of these quantities therefore provide valuable insight into the physiological and biophysical properties of the organism (Segrè et al., 2005; St Onge et al., 2007; Kinney et al., 2010; Costanzo et al., 2010).

With enough reconstructions, one can also obtain information about the larger-scale structure of the fitness landscape. For example, one can assess whether interactions between mutations are generally antagonistic or synergistic (Jasnos and Korona, 2007), or estimate the prevalence of sign epistasis (Weinreich et al., 2006) and overall levels of modularity (Segrè et al., 2005). These questions are typically quantified using statistical summaries of the microscopic epistasis (e.g., the distribution of pairwise epistasis values), which are aggregated over a large ensemble of mutations and genetic backgrounds. While the biological interpretation of these statistics is sometimes unclear, they can in principle exhibit regular and generalizable patterns. This makes them potentially amenable to comparison with simple fitness landscape models, such as Fisher’s geometrical model (Fisher, 1930), the uncorrelated landscape (Kingman, 1978; Kauffman and Levin, 1987), and the NK landscape (Kauffman and Weinberger, 1989). Yet while these statistics are designed to capture global properties of the fitness landscape, they are still fundamentally microscopic in nature, since they can only be estimated from microscopic (i.e. reconstruction-based) measurements. As such, they suffer from the same throughput limitations as any other reconstruction-based method, and one can only focus on a small subset of possible genotypes.

However, an evolving population typically explores a much larger number of genotypes than is feasible to re-

construct experimentally. The evolutionary dynamics depends on the entire *distribution* of fitness effects (“the DFE”), and on how this distribution varies among different genetic backgrounds. We denote this background-dependent DFE by $\rho(s|\vec{g})$: the fraction of mutations with fitness effect s in genetic background \vec{g} . In contrast to the statistics above, the background dependence of the DFE is a *macroscopic* form of epistasis, since it includes no information about the background-dependence of any individual mutation. Like many macroscopic quantities, there is not a one-to-one correspondence between the underlying microscopic epistasis and its macroscopic manifestation. For example, one can imagine a scenario where epistasis changes the identities of beneficial mutations after every substitution, but in a way that preserves the overall shape of the DFE. In this case, the widespread patterns of microscopic epistasis are masked at the macroscopic level, and the dynamics of adaptation will be indistinguishable from a nonepistatic scenario. At the opposite extreme, the DFE can change even without any microscopic epistasis once selection starts to deplete the finite supply of beneficial mutations. In this case, the dynamics of adaptation will show signatures of macroscopic epistasis even though there are no direct interactions between mutations.

Despite the potential importance of macroscopic epistasis in evolutionary adaptation, it remains less well-characterized than its microscopic counterpart. In principle, it is possible to measure the background dependence of the DFE directly, by assaying the fitness of large libraries of random mutants (Silander et al., 2007; MacLean et al., 2010; Miller et al., 2011; Bank et al., 2014). However, such studies suffer from similar throughput limitations as the microscopic approach above. These throughput limitations are compounded by the fact that the most important changes in the DFE, from an evolutionary perspective, are often located in difficult-to-sample regions such as the high-fitness tail (Good et al., 2012).

To avoid these issues, a number of studies have focused on the evolutionary outcomes themselves, associating observed differences in the adaptability of different strains with differences in the underlying DFE (Silander et al., 2007; Burch and Chao, 2000; Barrick et al., 2010; Woods et al., 2011; Kryazhimskiy et al., 2012; Perfeito et al., 2014; Kryazhimskiy et al., 2014). In principle, this approach offers the greatest sensitivity for detecting relevant differences in the DFE among related genetic backgrounds. However, it does so by transforming the measurement into an inverse problem: the patterns of macroscopic epistasis must ultimately be inferred from the dynamics of a few observable quantities (e.g. changes in fitness over time or across experimental treatments), which depend on the complex population genetics of an evolving microbial population (Lang et al., 2013; Frenkel et al., 2014). Thus, while it is easy to demonstrate the

existence of macroscopic epistasis with this approach, it is difficult to associate the observed differences in adaptability with the precise changes in the underlying DFE. This, in turn, has made it hard to distinguish between competing models of epistasis when interpreting the results of the experiment (Kryazhimskiy et al., 2014; Frank, 2014).

In the present manuscript, we propose a general framework for quantifying patterns of macroscopic epistasis from observed differences in adaptability. We then use this framework to investigate the role of epistasis in a well-studied laboratory evolution experiment in *E. coli* (Wiser et al., 2013). By analyzing the differences in the dynamics of adaptation through time, we can make inferences about the changes in the DFE that have accumulated over the course of the experiment. These changes constitute the most basic form of epistasis that arises during adaptation to a constant environment. Similar to Kryazhimskiy et al. (2009), we focus on two simple summaries of the dynamics: the competitive fitness and the total number of genetic changes relative to the ancestor. We use a combination of theory and numerical simulations to investigate how well these data are explained by several popular models of macroscopic epistasis, including the recently proposed diminishing returns model of Wiser et al. (2013). We find that fitness measurements alone have little power to discriminate between different models of epistasis, while the addition of genetic information is sufficient to rule out many existing explanations of the data. Together, these results highlight the need for more sophisticated models of macroscopic epistasis that are compatible with *all* of the experimental data, as well as additional DNA sequence data to test their predictions.

RESULTS

Fitness and mutation trajectories in the LTEE

In the long-term evolution experiment (LTEE) conducted by Lenski and collaborators, twelve populations of *Escherichia coli* were founded from a single common ancestor (Lenski et al., 1991) and propagated in a constant environment for more than 60,000 generations (see Wiser et al. (2013) for a recent summary of experimental details). A central observable quantity is the fitness of the evolved populations, which can be measured using competition assays with a marked ancestor. If f_i and f_f denote the frequencies of the evolved strain at the beginning and end of the competition assay, then the (log)-fitness, X , is given by

$$X \equiv \frac{1}{\Delta t} \log \left[\frac{f_f}{1 - f_f} \frac{1 - f_i}{f_i} \right], \quad (1)$$

where Δt is the duration of the competition in generations. Note that this definition of fitness differs from the traditional measure W reported in previous studies of the LTEE. Although the two measures are correlated, Eq. (1) provides a more direct connection to the population genetic theory described in the following sections.

Using the fitness assays reported in Wiser et al. (2013), we calculated the fitness defined by Eq. (1) for each population at approximately 40 timepoints during the first 50,000 generations of evolution (see Methods). We plot the fitness trajectories for the six complete, non-mutator populations in Fig. 1A. Measurement error estimated from replicate assays is substantial ($\text{stderr} \sim 3\%$, Fig. 1C), leaving us with little power to distinguish fluctuations in individual trajectories. Instead, we pool all six populations and focus on the *average fitness trajectory* $\bar{X}(t)$ (Fig. 1B). Bootstrap resampling from the errors in Fig. 1C suggests that the measurement error in $\bar{X}(t)$ is smaller ($\text{stderr} \sim 1\%$) and more normally distributed (Fig. 1D). However, even for the average fitness trajectory, the fluctuations between neighboring timepoints still fall within experimental uncertainty, so we can only obtain robust inferences from long-term trends in the data.

The most striking trend is the pronounced slowdown in the rate of adaptation during the course of the experiment: nearly two-thirds of the total fitness was gained in the first 5,000 generations of evolution. This deceleration is inconsistent with a constant DFE, which would predict that fitness increases linearly with time, on average. Instead, the slowdown in the rate of adaptation has long been interpreted as a signature of *diminishing returns epistasis*, consistent with the approach to a fitness plateau (Lenski and Travisano, 1994). Previous work has argued that the shape of the deceleration is best captured by a logarithmic fitness trajectory,

$$\bar{X}(t) = X_c \log \left(1 + \frac{v_0 t}{X_c} \right), \quad (2)$$

where v_0 gives the initial rate of fitness increase and X_c controls the severity of the slowdown (Wiser et al., 2013; Kryazhimskiy et al., 2009; Sibani et al., 1998); the best-fit parameters are shown in Fig. 1B. The shape of this trajectory has been used to argue that fitness is still increasing in the LTEE (Wiser et al., 2013), rather than asymptoting to a fitness peak (Lenski and Travisano, 1994).

More recent work has tried to use the shape of the fitness trajectory to make inferences about the underlying model of epistasis in the LTEE (Frank, 2014; Wiser et al., 2013; Kryazhimskiy et al., 2009). However, to truly distinguish between different models, we must move beyond the simple curve fitting implied by Eq. (2) and postulate a set of concrete population genetic models that can be used to generate predictions for $\bar{X}(t)$. The likelihood of the observed fitness trajectory can then be written in the

form

$$p(\bar{X}_{\text{obs}}|\theta) = \int p_{\text{err}}(\bar{X}_{\text{obs}} - \bar{X}) \cdot p_{\text{evol}}(\bar{X}|\theta) d\bar{X}. \quad (3)$$

Here, $p_{\text{evol}}(\bar{X}|\theta)$ is the probability distribution of $\bar{X}(t)$ in the underlying model, which depends on some set of parameters θ , and $p_{\text{err}}(\bar{\epsilon})$ is the distribution of measurement errors, which we assume to be normally distributed with variance $\sigma_{\text{err}} \approx 1.4\%$ (Fig. 1D). By computing this likelihood, we can assess the fit of a given model using standard statistical techniques (see Methods). In contrast to the curve-fitting approach of earlier work, this method correctly accounts for inherent stochasticity of the evolutionary process, which can lead to correlated fluctuations in the observed fitness trajectory. Yet in practice, it is often difficult to compute the likelihood in Eq. (3) because the model distribution $p_{\text{evol}}(\bar{X}|\theta)$ is unknown. This is largely due to the large population size of the LTEE ($N \approx 3 \times 10^7$), which makes it difficult to analyze even the simplest population genetic models (Desai and Fisher, 2007). To avoid these issues, we use computer simulations of the model to obtain accurate predictions of the fitness trajectory (see Methods), computing the approximate likelihood function as

$$p(\bar{X}_{\text{obs}}|\theta) \approx \frac{1}{n} \sum_{i=1}^n p_{\text{err}}(\bar{X}_{\text{obs}} - \bar{X}_{\text{sim}(\theta),i}). \quad (4)$$

Unfortunately, regardless of the method used for inference, we will demonstrate that there is little power to distinguish between different models of epistasis based on the fitness trajectory alone. As noted by Frank (2014), it is relatively easy to devise an epistatic model that reproduces the observed fitness trajectory in Fig. 1B, and we outline several specific examples below. Fortunately, the average fitness trajectory is not the only quantity that has been measured in the LTEE. DNA sequences from a small number of clones are available for several timepoints in a subset of the lines (Barrick et al., 2009; Wielgoss et al., 2011, 2013). Although this genetic data is more sparse than the fitness measurements, it provides a crucial window into the molecular changes responsible for the observed patterns of fitness evolution. In Fig. 1B, we plot the average number of genetic differences between the ancestor and a set of clones sampled from the non-mutator populations (see Methods). When viewed as a function of time, this *mutational trajectory* $\bar{M}(t)$ is the natural genetic analogue of the average fitness trajectory $\bar{X}(t)$. Any evolutionary model which purports to explain the long term trends in $\bar{X}(t)$ must also be consistent with the observed values of $\bar{M}(t)$. As we will see below, this turns out to be much more informative than fitting the fitness trajectory on its own.

The most striking feature of the mutation trajectory in Fig. 1 is the sheer number of mutations that have accumulated during the experiment. Although the full data

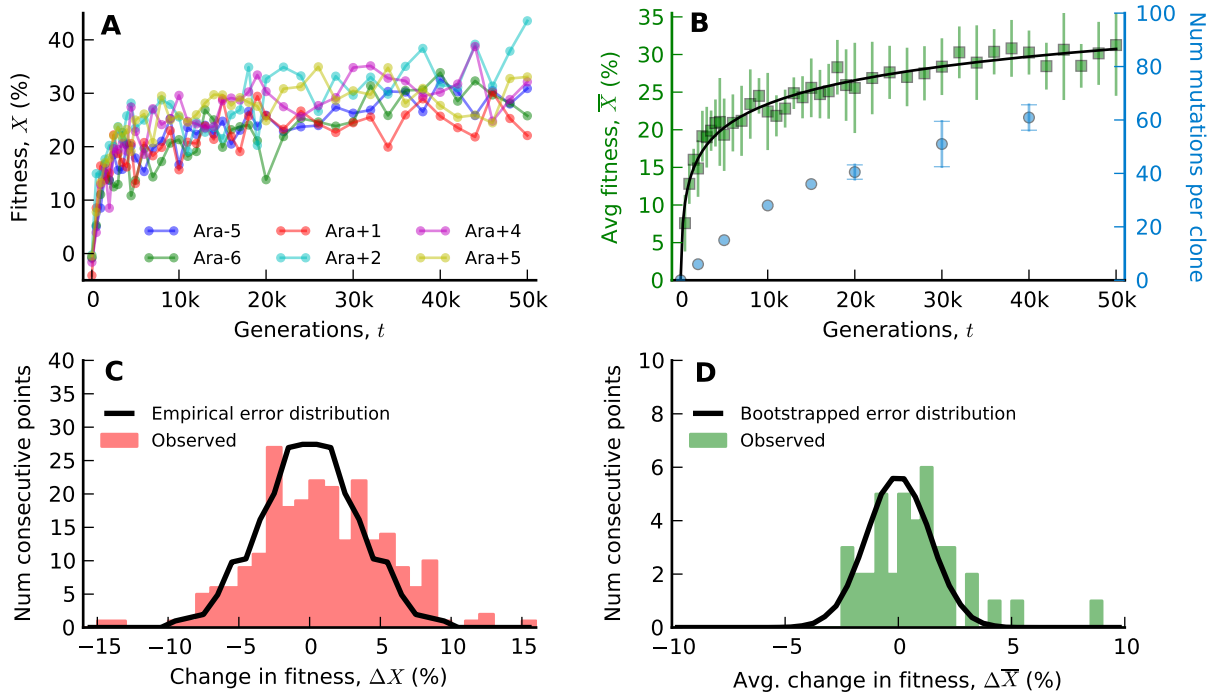


FIG. 1 Fitness and mutation trajectories in the LTEE. (A) Individual fitness trajectories for the six complete, non-mutator populations analyzed by Wisser et al. (2013). Each point is the average of two independent competition assays, with fitness estimated from Eq. (1). (B) The average fitness trajectory for the six populations in panel A (green squares), with ± 2 stderr confidence intervals. For comparison, the solid line depicts the logarithmic trajectory in Eq. (2), with estimated parameters $X_c \approx 4.6 \times 10^{-2}$ and $v_0 \approx 7.7 \times 10^{-4}$. The blue circles depict the average number of mutations in single clones sampled from the LTEE (see Methods), ± 2 stderr confidence intervals for timepoints with more than one sampled clone. (C) The change in fitness between consecutive timepoints, pooled across all six populations in panel A. The black curve shows the empirical distribution of measurement errors, defined as half of the difference between replicate fitness measurements. (D) The average change in fitness between consecutive timepoints. The black curve shows the bootstrapped distribution of measurement errors, obtained by repeatedly averaging six randomly chosen errors from the empirical distribution in panel C. The standard deviation of this distribution is $\sigma_{\text{err}} \approx 1.4\%$.

no longer support the constant substitution rate observed in the first 10,000 generations of evolution (Barrick et al., 2009), the number of mutations in the later portion of the experiment is still much higher than one might expect based on the fitness trajectory. Roughly half of all mutations accumulated *after* the first 10,000 generations, when rate of fitness increase had already slowed substantially. Of course, some unknown fraction of these mutations are likely to be selectively neutral, as these are expected to accumulate continuously at the neutral mutation rate U_n (Barrick et al., 2009). However, the number of synonymous mutations suggests that the total mutation rate in these strains is approximately $U_{\text{tot}} \sim 4 \times 10^{-4}$ (Wielgoss et al., 2011), implying that the majority of the mutations in Fig. 1 must be beneficial. In fact, the substitution rate in the first 10,000 generations is so rapid that many of these beneficial mutations must be segregating in the population at the same time. Given that the typical fitness effect of a fixed mutation is at most about 10% (Khan et al., 2011), the fixation time of a successful mutation is much longer than the maximum possible

waiting time between mutations. As a result, these mutations must compete for fixation within the population — a process known as *clonal interference* (Desai and Fisher, 2007; Gerrish and Lenski, 1998). This will prove to be an important factor in the theoretical analysis below.

Macroscopic epistasis from a finite genome

Although a decelerating fitness trajectory is a clear signature of *macroscopic* epistasis (i.e., a changing DFE), this does not necessarily imply that *microscopic* epistasis must be at work. The DFE can change even in the absence of epistasis provided that the length of the genome is finite. Given enough time, the population will eventually exhaust the supply of beneficial mutations, and the rate of adaptation will slow substantially. Thus, this nonepistatic scenario offers one of the simplest possible explanations for the decelerating rate of adaptation in the LTEE, provided that it can also *quantitatively* reproduce the trajectories in Fig. 1.

In the simplest version of this model, the instantaneous change in the beneficial DFE is given by

$$L\partial_t\rho(s,t) = -NU\rho(s,t)p_{\text{fix}}(s), \quad (5)$$

where L is the length of the genome and $p_{\text{fix}}(s)$ is the fixation probability of a new mutation. Equation (5) accounts for the fact that, once a beneficial mutation fixes, a second mutation at that site is not likely to be beneficial, effectively removing this site from the DFE. In a true “finite sites” model, each of the L beneficial mutations corresponds to a single site in the genome, and the ratio U/L is set by the per-site mutation rate μ . However, Eq. (5) also describes the evolution of the DFE in generalized “running out of mutations” model — for example, there could be L genes which are beneficial to knock out, or L modules to improve (Kryazhimskiy et al., 2014; Tenaillon et al., 2012). In these cases, L represents the total number of non-redundant mutations (e.g. the number of genes to knock out), and U/L is the average target size. The rate of change of the DFE in Eq. (5) is inversely proportional to L , and it vanishes in the limit that $L \rightarrow \infty$ as expected.

Given a solution for the time-dependent DFE in Eq. (5), the expected fitness and mutation trajectories are given by

$$\partial_t\bar{X}(t) = \int sNU\rho(s,t)p_{\text{fix}}(s)ds, \quad (6a)$$

$$\partial_t\bar{M}(t) = \int NU\rho(s,t)p_{\text{fix}}(s)ds. \quad (6b)$$

Unfortunately, both Equations (5) and (6) are difficult to solve in general, since the fixation probability also depends on the DFE (Good et al., 2012). Despite this difficulty, we can gain considerable qualitative insight by focusing on the strong-selection, weak-mutation (SSWM) limit, where the fixation probability is given by Haldane’s formula, $p_{\text{fix}}(s) \approx 2s$ (Haldane, 1927). In this limit, the evolution of the DFE greatly simplifies: deleterious mutations can be neglected, and the distribution of beneficial fitness effects is given by

$$\rho(s,t) = \rho_0(s)e^{-2NUst/L}, \quad (7)$$

where $\rho_0(s)$ is the DFE in the ancestral background. The average fitness and mutation trajectories can then be obtained by substituting Eq. (7) into Eq. (6) and evaluating the resulting integral. For example, arguments from extreme value theory suggest that the ancestral DFE may often be exponential (Gillespie, 1984; Orr, 2002), which leads to an average fitness trajectory of the form

$$\bar{X}(t) = X_c \left[1 - \left(1 + \frac{v_0 t}{2X_c} \right)^{-2} \right], \quad (8)$$

where $v_0 = 2NU \int s^2 \rho_0(s) ds$ and $X_c = L \int s \rho_0(s) ds$. However, this trajectory predicts a much sharper deceleration in the adaptation rate than is observed in Fig. 1 (Fig. S1).

More generally, we find that the adaptation rate for the DFE in Eq. (7) is proportional to the Laplace transform of $s^{-2}\rho_0(s)$, which leads to an inverse relation of the form

$$\rho_0(s) = \frac{1}{Ls^2} \mathcal{L}^{-1} \{ \partial_t \bar{X}(t) \} \left(\frac{2NUs}{L} \right). \quad (9)$$

In other words, the finite-sites model can reproduce an *arbitrary* fitness trajectory¹ provided that the ancestral DFE satisfies Eq. (9). For example, the logarithmic fitness trajectory in Eq. (2) corresponds to an ancestral DFE of the form

$$\rho_0(s) \propto \begin{cases} s^{-2}e^{-s/\sigma} & s > \sigma\epsilon \\ 0 & s \leq \sigma\epsilon, \end{cases} \quad (10)$$

where $\epsilon \ll X_c/v_0 t_{\text{max}}$ is a lower cutoff chosen to maintain normalization. The fitting parameters in Eq. (2) are given by $X_c = L\sigma\epsilon$ and $v_0 = 2NU\epsilon\sigma^2$.

A similar argument shows that we can also reproduce an arbitrary *mutation* trajectory, provided that the ancestral DFE satisfies

$$\rho_0(s) = \frac{1}{Ls} \mathcal{L}^{-1} \{ \partial_t \bar{M}(t) \} \left(\frac{2NUs}{L} \right). \quad (11)$$

However, while we can fit arbitrary fitness or mutation trajectories by choosing the appropriate ancestral DFE, it is not possible to fit both quantities at the same time. In the weak mutation limit, the average fitness and mutation trajectories in the finite sites model are related by

$$\bar{M}(t) = 2N \left(\frac{U}{L} \right) \int_0^t [\bar{X}(\infty) - \bar{X}(\tau)] d\tau, \quad (12)$$

regardless of the choice of ancestral DFE. By choosing $\rho_0(s)$ to fit the fitness trajectory, we completely determine the mutation trajectory, and vice versa. For example, the logarithmic fitness trajectory in Eq. (2) implies a constant substitution rate

$$\bar{M}(t) \approx \frac{v_0 t}{2N \langle s \rangle_f \left(\frac{U}{L} \right)}, \quad (13)$$

where $\langle s \rangle_f \approx \sigma / \log(1/\epsilon)$. This linear increase is inconsistent with the mutation trajectory in Fig. 1, which starts to show deviations from linearity after generation 10,000.

However, a potential caveat with this analysis is that the mutation trajectory in Eq. (13) (and much of the analysis preceding it) depends on our assumption of the weak-mutation limit ($NU \ll 1$). This is often not self-consistent: in the LTEE, the weak-mutation analysis typically leads us to infer parameter values that violate the

¹ Strictly speaking, the fitness trajectory must be such that the rate of adaptation can be written as the Laplace transform of some function.

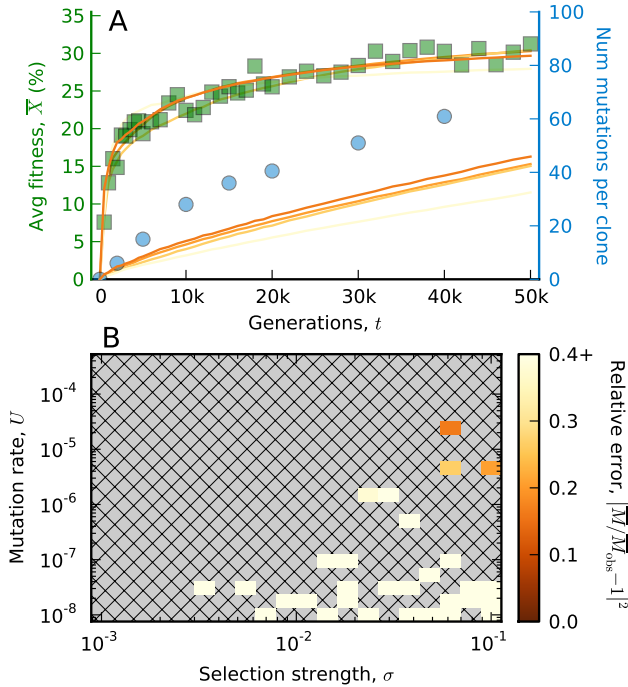


FIG. 2 Fitting a finite sites model to the LTEE. (A) Simulated fitness and mutation trajectories for the ancestral DFE in Eq. (10) with $\epsilon = 3 \times 10^{-4}$ (solid lines). We have included all simulated combinations of U , σ , and L with $p > 0.05$ and $|\bar{M}/\bar{M}_{\text{obs}} - 1|^2 < 0.04$. Each line is colored according to the relative error of the mutation trajectory, $|\bar{M}/\bar{M}_{\text{obs}} - 1|^2$, after fitting the best-fit neutral mutation rate $0 < U_n < U_{\text{tot}}$ by least-squares. For comparison, we have also included the observed fitness and mutation trajectories from Fig. 1B. (B) The relative error of the mutation trajectory for all simulated parameter combinations. For each combination of U and σ , we plot the minimum error across all simulated values of L , and we have only included parameter combinations for which $p > 0.05$.

weak-mutation assumptions. For example, in the finite-sites model defined by Eq. (10), the fitted values of X_c and v_0 in Fig. 1 require that $NU \geq 3$, which violates the weak-mutation condition used to derive Eqs. (10) and (13). Thus, we must turn to our computational framework to rigorously compare this model with the data.

To do so, we performed a grid search over combinations of U , L , and σ for the ancestral DFE defined by Eq. (10). The posterior predictive p -value for this model is $p \approx 0.9$ (χ^2 test, see Methods), which shows that the finite-sites model can still reproduce the observed fitness trajectory in the presence of clonal interference. Figure 2 shows the average fitness and mutation trajectories for all parameters with $p > 0.05$. The mutation trajectories also include a best-fit rate of neutral mutations ($0 \leq U_n \leq U_{\text{tot}} - U$) which is fit to minimize the mean squared error from the observed mutation trajectory. Even with this correction, the mutation trajectories

remain inconsistent with the data, which allows us to reject the simple finite sites model in Eq. (5).

Fitness trajectories on an uncorrelated fitness landscape

We next consider an alternative model of macroscopic epistasis — the *uncorrelated fitness landscape* — which represents the opposite limit of the additive finite-genome models above (Kingman, 1978; Kauffman and Levin, 1987; Gillespie, 1984; Orr, 2002). In this model, the fitness of every genotype is drawn independently from the same distribution $f(X)$. In our notation, this implies that the DFE is given by

$$\rho(s|\vec{g}) = f(X(\vec{g}) + s), \quad (14)$$

where $X(\vec{g})$ denotes the fitness of genotype \vec{g} . This uncorrelated landscape contains extensive microscopic epistasis, with the standard deviation of the pairwise epistasis $\epsilon_{ij} = s_{ij} - s_i - s_j$ on the same order as s_i . The fitness effect of a given mutation is therefore barely heritable. However, much of this idiosyncratic microscopic epistasis averages out at the level of the DFE, which depends on the genetic background only through the fitness $X(\vec{g})$.

The dynamics of adaptation become particularly simple when $f(X)$ is exponentially distributed, since the beneficial portion of the DFE remains exponential (with the same mean) regardless of the fitness. Instead, epistasis primarily acts to reduce the beneficial mutation rate via $U_b(X) = Ue^{-X/\sigma}$, where σ is the average fitness effect in the ancestral background. In the weak-mutation limit, this diminishing mutation rate leads to the same logarithmic fitness trajectory as Eq. (2), with $X_c = \sigma$ and $v_0 = 4NU_b\sigma^2$ (Kryazhimskiy et al., 2009). Thus, the fitnesses in Fig. 1 can also be reproduced in this model of extreme epistasis, in addition to the purely additive model in Eq. (10). However, the corresponding mutation trajectory,

$$\bar{M}(t) = \log \left(1 + \frac{v_0 t}{X_c} \right), \quad (15)$$

contains no free parameters. This form of $\bar{M}(t)$ implies a substitution rate of essentially zero after $t \sim X_c/v_0$ generations, which is clearly inconsistent with the data (Figs S2 and S3). Thus, while the fitness trajectory is consistent with an uncorrelated landscape, this model is again unable to reproduce the observed mutation trajectory.

Global fitness-mediated epistasis

The general patterns of macroscopic epistasis in the uncorrelated landscape can also be realized in other models which have much less microscopic epistasis. For example,

a key simplifying assumption of the uncorrelated landscape is that the effective beneficial mutation rate only depends on the fitness of the genetic background and not on its specific genotype. This leads us to consider a broader class of models of the form

$$\rho(s|\vec{g}) = \rho(s|X(\vec{g})), \quad (16)$$

where the shape of the DFE is similarly mediated by fitness. This form of epistasis has been implicated in recent genetic reconstruction studies (Kryazhimskiy et al., 2014; Khan et al., 2011; Chou et al., 2011), and it has been hypothesized to describe the patterns of epistasis in the LTEE as well (Wiser et al., 2013). These studies have focused on an even simpler class of models of the form

$$\rho(s|X) = f(X)^{-1} \rho_0(s/f(X)), \quad (17)$$

where the fitness-dependence of the DFE is given by a simple change of scale. We assume by convention that $f(0) = 1$, so that $\rho_0(s)$ represents the ancestral DFE. In the weak mutation limit, the fitness trajectories for Eq. (17) must satisfy the implicit relation

$$t(\bar{X}) = \frac{1}{v_0} \int_0^{\bar{X}} \frac{dX}{f(X)^2}, \quad (18)$$

where $v_0 = 2NU \int s^2 \rho_0(s) ds$. We can then invert this equation to solve for $f(X)$ as a function of the fitness trajectory:

$$f(X) = \sqrt{\frac{1}{v_0} \frac{d\bar{X}}{dt}} \bigg|_{t=\bar{X}^{-1}(X)} \quad (19)$$

Thus, like the finite-sites model above, we can reproduce an *arbitrary* fitness trajectory with the rescaled DFE in Eq. (17) by choosing the correct form for $f(X)$.

We can realize this model microscopically by assuming that fitness effects of individual mutations obey the same scaling relation,

$$s(X) = s_0 f(X), \quad (20)$$

which allows us to make predictions for microscopic quantities like the fitness effects of reconstructed strains. However, there is not complete freedom to choose $f(X)$ in this microscopic model, since the combined effects of a sequence of mutations must commute with each other. The only rescaling that satisfies this commutative property is the linear relation $f(X) = 1 - X/X_c$, where X_c represents the global fitness maximum. In this case, the fitness effect of each mutation is scaled by the fractional distance to the peak, similar to the “stick-breaking” model of Nagel et al. (2012). In the weak-mutation limit, this model reproduces the hyperbolic fitness trajectory

$$\bar{X}(t) = v_0 t \left(1 + \frac{v_0 t}{X_c} \right)^{-1}, \quad (21)$$

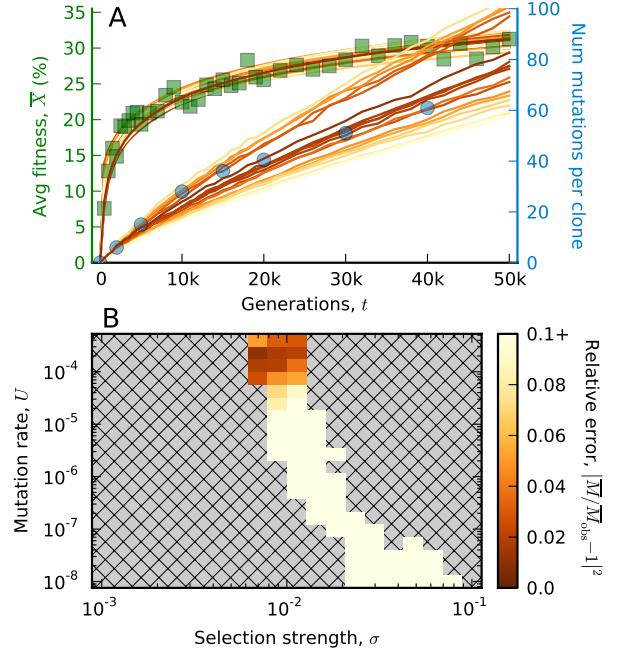


FIG. 3 Fitting a fitness-mediated epistasis model to the LTEE data. An analogous version of Fig. 2 constructed for the global diminishing returns model in Eq. (22) with an exponential ancestral DFE. Note the change in scale for the relative error in the mutation trajectory.

which has been used to fit the LTEE fitness data in previous studies (Lenski and Travisano, 1994). However, as shown by Wiser et al. (2013), Eq. (21) provides a relatively poor fit to the observed fitness trajectory (Fig. S1), even after accounting for clonal interference (posterior predictive $p < 10^{-3}$). This allows us to rule out all microscopic models of the form in Eq. (20).

For other choices of $f(X)$, Eq. (17) will hold only in a statistical sense, with a more complicated pattern of microscopic epistasis than predicted by Eq. (20). Wiser et al. (2013) have shown that the logarithmic fitness trajectory in Eq. (2) can be recovered by setting

$$f(X) = e^{-X/2X_c}. \quad (22)$$

However, like the additive and uncorrelated models above, the mutation trajectory in this case is strongly constrained by $\bar{X}(t)$. In the weak mutation limit, the mutation trajectories for Eq. (17) must satisfy

$$\bar{M}(t) = \frac{\sqrt{v_0}}{\langle s \rangle_f} \int_0^t \left(\frac{d\bar{X}}{dt} \right)^{1/2} dt, \quad (23)$$

where $\langle s \rangle_f = \int s^2 \rho_0(s) ds / \int s \rho_0(s) ds$ is the average fitness effect of the first fixed mutation. For the logarithmic fitness trajectory in Eq. (2), the corresponding mutation trajectory grows as a square root of time:

$$\bar{M}(t) = \frac{2X_c}{\langle s \rangle_f} \left(\sqrt{1 + \frac{v_0 t}{X_c}} - 1 \right), \quad (24)$$

with only an overall scale $\langle s \rangle_f$ that can be tuned to fit the data. At first glance, Eq. (24) appears to give a decent fit to the observed mutation trajectory (Fig. S2), although it systematically overestimates the curvature. However, the best-fit scale $\langle s \rangle_f \sim 5\%$ lies in the clonal interference regime, so we must again turn to our computational framework to rigorously compare this model with the data.

To do so, we performed a grid search over combinations of U , σ , and X_c for an exponential ancestral DFE, $\rho_0(s) \propto \exp(-s/\sigma)$. The posterior predictive p -value is $p \approx 0.9$, which shows that this model can still reproduce the observed fitness trajectory even when $NU > 1$. Figure 3A shows the average fitness and mutation trajectories for all parameters with $p > 0.05$. As expected, there is a large “ridge” of parameter values that reproduce the observed fitness trajectory, but the vast majority of these parameter combinations are inconsistent with the observed mutation trajectory. Those parameters with the best estimates of $\bar{M}(t)$ still display some systematic errors (Fig. 3B), underestimating the number of mutations in the first part of the experiment and overestimating them later. The numerical values of these parameters are also wildly unrealistic (e.g., predicting that a quarter of all genomic mutations have beneficial fitness effects greater than 1%). In light of this information, we conclude that the mutation data is inconsistent with the particular global diminishing returns model proposed by Wisner et al. (2013).

However, previous theoretical work suggests that the precise value of the estimated mutation rate can dramatically vary with the shape of the ancestral DFE (Good et al., 2012), while the predictions of Eq. (18) are insensitive to this choice. In accordance with this intuition, the inferred parameters become more realistic if we truncate the exponential distribution at $s_{\max} = 4\sigma$, although the systematic errors in the mutation trajectory remain (Fig. S4). Compared to the finite-sites model and uncorrelated landscape above (as well as the original Wisner *et al* model), this modified version of the global diminishing returns model is the only one that can plausibly reproduce *all* of the observed data.

Evidence for two evolutionary epochs

While the discrepancies in the mutation trajectory are too small to reject the fitness-mediated epistasis model outright, these systematic errors still suggest that the model defined by Eq. (22) is missing a key feature of the experiment. This argues for a degree of caution in interpreting the parameters inferred in Fig. 3, particularly far into the future where the errors in the fitness and mutation trajectories start to grow larger. Of course, we could continue to postulate more elaborate models of epistasis to account for the mutation trajectory, and with

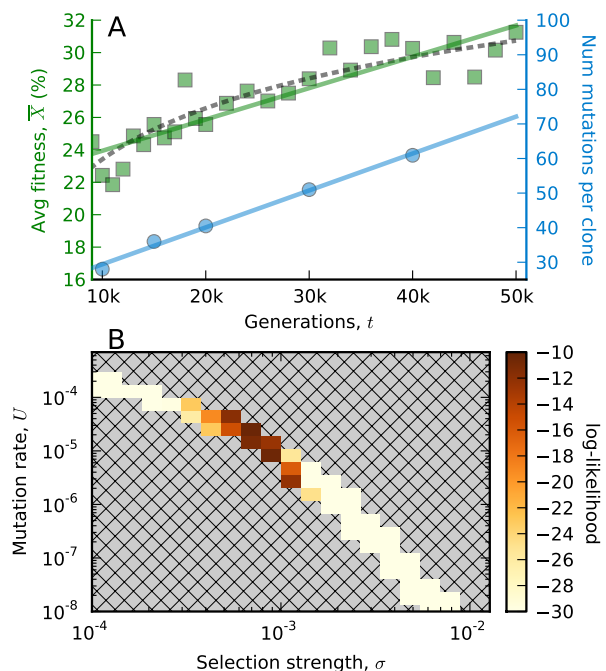


FIG. 4 Fitting a nonepistatic model to the last 40,000 generations of evolution. (A) The average fitness and mutation trajectories from Fig. 1C, along with the predictions of the nonepistatic curve in Eq. (25) (solid lines). The estimated parameters are $v_0 \approx 1.9 \times 10^{-6}$ and $R_0 \approx 1.1 \times 10^{-3}$. For comparison, we have also included the best-fit logarithmic trajectory from Eq. (2) (dashed line). (B) The likelihood of the fitness trajectory for a constant, exponential DFE truncated at $s_{\max} \approx 4\sigma$, with a y -intercept fitted using maximum likelihood. We have only included parameters whose substitution rates are consistent with the observed mutation trajectory ($R_0 - U_{\text{tot}} \leq \partial_t \bar{M} \leq R_0$).

enough additional parameters this approach is likely to be successful. But without a biological basis for choosing among the space of possible models, these additional assumptions are likely to overfit the mutation trajectory and lead to incorrect predictions for other observables (e.g., genetic diversity or variation among lines). Instead, we focus on an alternative class of models that are simpler in some ways, though more complex in others.

Revisiting the original data in Fig. 1, we note that we were initially led to consider models of macroscopic epistasis, rather than a constant DFE, because of the differences between the initial part of the experiment (i.e., before generation 10,000) and the remaining 40,000 generations. This suggests a model of epistasis with two evolutionary epochs: an initial “poorly adapted” phase in the first 10,000 generations followed by a more “well-adapted” phase for the remaining 40,000 generations. We do not attempt to model the initial phase, but instead simply assume that the population is subject to some complicated and unspecified model of epistasis that generates the observed data with probability one. This could

account for the fact that the large-effect mutations available at the beginning of the experiment might depend on specific details of the ancestral strain or other experimental details. After this initial phase of adaptation is complete, the population enters a second phase of evolution with negligible macroscopic epistasis. In other words, rather than try to fit a single model of a changing DFE to the whole experiment, we neglect the first 10,000 generations and instead try to fit an evolutionary model with a *constant* DFE to the last 40,000 generations of evolution.

Assuming a constant DFE implies that the fitness and mutation trajectories after generation 10,000 are given by

$$\overline{X}(t) = v_0 t + X_c, \quad \overline{M}(t) = R_0 t + M_c. \quad (25)$$

This fitness trajectory has the same number of parameters as the logarithmic curve in Eq. (2), and we see that even on a purely curve-fitting level, the nonepistatic fitness trajectory is only marginally less accurate than its epistatic counterpart (Fig. 4). We infer an adaptation rate of $v_0 \approx 0.2\%$ per 1000 generations and a substitution rate of $R_0 \approx 1.1$ per 1000 generations. Although this adaptation rate appears to overestimate the fitness gain after generation 40,000, additional fitness assays performed between generations 40,000 and 50,000 corroborate the 2% increase (Wiser et al. (2013), Fig. S5). The fitted values of v_0 and R_0 can be used to infer the typical fitness effect of a fixed mutation and a corresponding effective mutation rate based on the relations

$$s_{\text{eff}} \approx \frac{v_0}{R_0}, \quad v_0 \approx \frac{2 \log(2N s_{\text{eff}})}{\log^2(s_{\text{eff}}/U_{\text{eff}})}, \quad (26)$$

derived in previous theoretical work (Desai and Fisher, 2007). For the values of v_0 and R_0 above, we find a typical fixed fitness effect of order $s_{\text{eff}} \sim 2 \times 10^{-3}$ and an effective mutation rate of order $U_{\text{eff}} \sim 2 \times 10^{-6}$.

However, this discussion has so far been based purely on curve-fitting and not on a specific generative model of the dynamics. Using our computational framework, we can evaluate the fit of the two-epoch model more rigorously and obtain more precise estimates of the underlying parameters. To do so, we performed a grid search over combinations of U , σ , and X_c for a truncated exponential distribution ($s_{\text{max}} = 4\sigma$) which can be directly compared to the best-fit diminishing returns model in Eq. (22). We find that the best nonepistatic models provide a marginally better fit to the average fitness trajectory than the best-fit diminishing returns model, and a significantly better fit to the mutation trajectory (Fig. 4). This suggests that the nonepistatic model provides a much better fit to the data in the latter 40,000 generations of the experiment.

DISCUSSION

Genetic reconstructions provide numerous examples of interactions between the fitness effects of individual mutations. The existence of these interactions is hardly surprising, given the physiological and developmental complexity of most organisms. However, the evolutionary implications of these interactions remain controversial. In this study, we used longitudinal data from a long-term evolution experiment in *E. coli* to investigate the evolutionary influence of epistasis in a simple empirical setting. We focused on two basic questions: (1) how do naturally occurring patterns of epistasis alter the rate of fitness increase and the accumulation of new mutations in a constant environment? and (2) what are the simplest models of epistasis that are consistent with the observed data?

The first of these questions is largely descriptive, and has been the focus of previous work in this experimental system and many others (Silander et al., 2007; Kryazhimskiy et al., 2012; Perfeito et al., 2014; Kryazhimskiy et al., 2014; Wiser et al., 2013; Lenski and Travisano, 1994; Barrick et al., 2009; Wichman et al., 1999). The latter question, in contrast, demands a quantitative approach, and must account for the fact that the underlying model of epistasis can only be observed through the filter of population genetic stochasticity and measurement error. In this study, we developed a computational framework to account for these confounding factors, which allows us to quantify the consistency of a predicted fitness trajectory using well-established statistical tools. Combined with analytical results in the weak-mutation limit, we used this framework to investigate the compatibility of several popular models of epistasis.

We found that the shape of the fitness trajectory on its own provides little power to distinguish between different models of epistasis, including finite-sites models that lack any direct interactions between mutations. This suggests that the underlying “symmetry group” or universality class for this observable may be quite large (Frank, 2014), which could potentially explain why previous studies have been so successful at fitting the LTEE fitness trajectory with simple epistatic models (Frank, 2014; Wiser et al., 2013; Sibani et al., 1998). However, this symmetry is broken as soon as we include information about the number of mutations that have accumulated, and the *combination* of fitness and genetic data places much stronger constraints on the set of possible models. Of the simple 2 and 3-parameter models considered here, we found that a variant of the global diminishing returns model proposed by Wiser et al. (2013) provides the best fit to the observed data, although significant systematic errors remain. These systematic errors, combined with the weak-diminishing returns signal in the first five mutations in Ara-1 (Fig. S6) (Khan et al., 2011; Draghi and Plotkin, 2013), suggest a degree of caution in interpreting

the support for this model.

Instead, we find that the data may be better explained by a two-epoch model of adaptation, in which an initial burst of macroscopic epistasis is followed by a steady accumulation of mutations under a constant DFE. Although this model offers no insight into the initial (presumably idiosyncratic) phase of adaptation, it provides a more parsimonious explanation for the dynamics in the latter phase of the experiment. Moreover, given that this second phase accounts for $\sim 80\%$ of the present duration of the LTEE and more than half of the accumulated mutations, it could be argued that it provides a better description of the “typical” dynamics of adaptation in a constant environment than the initial, epistatic phase of the adaptive walk. Under this hypothesis, the widespread diminishing returns epistasis observed in other experimental systems may simply be a reflection of their comparatively brief duration.

In light of this speculation, it is worth commenting on the population genetic parameters estimated in the second, slower phase of the LTEE. When faced with a constant environment, it is natural to expect that a population will eventually enter a slower phase of adaptation once the most obvious beneficial mutations are exhausted. However, this steady-state is usually assumed to have a negligible beneficial mutation rate and correspondingly simple evolutionary dynamics. In contrast, the scaled mutation rates that we estimate for the LTEE are surprisingly large ($NU \sim 10 - 100$), and are comparable to rapidly evolving laboratory yeast populations near the beginning of their adaptive walk (Frenkel et al., 2014). Although the fitness effects of these mutations ($s \sim 0.1\%$) fall below the resolution limit of most fitness assays, the effective population size is large enough that the scaled selection strengths are quite large from a population genetic standpoint ($Ns \gtrsim 10^4$). Interestingly, these scaled beneficial mutation rates and selection strengths are sufficiently large that deleterious mutations are expected to have a negligible influence on the rate of adaptation. (We also note that extrapolating these estimates to the mutator lines would suggest that the declining mutation rate observed in Ara-1 (Wielgoss et al., 2013) may involve selection for more than just a reduced deleterious load.)

Together, these estimates suggest that even the “slow” phase of the LTEE is characterized by rapid adaptation, in which multiple beneficial mutations compete for fixation at the same time. These dynamics are illustrated by the simulated mutation trajectories in Fig. S7, which display an even greater amount of hitchhiking and clonal interference than similar trajectories measured in a recent evolution experiment in yeast (Lang et al., 2013). However, since the individual fitness effects are an order of magnitude smaller, the competition between beneficial mutations occurs over a much longer timescale than is normally observed in experimental evolution. For ex-

ample, it is not uncommon to find a beneficial mutation that persists for thousands of generations at intermediate frequencies before it accumulates enough additional mutations to sweep to fixation. These transiently stable polymorphisms would suggest adaptive radiation or frequency-dependent selection on a more traditional experimental timescale (e.g. less than 2,000 generations), but they arise here as a natural consequence of the population genetic process.

Of course, the preceding discussion should be treated with a degree of caution, since our present estimates are based on a limited number of clone sequences and relatively noisy fitness measurements. It is possible that additional data would indicate a departure from the constant adaptation rate in the second phase of the experiment, or reverse some of the systematic errors of the global diminishing returns model. Moreover, even a perfectly resolved fitness and mutation trajectory will likely be consistent with more than one evolutionary model, just as a perfectly resolved fitness trajectory is consistent with multiple mutation trajectories. Our estimates should therefore be viewed as merely consistent with the available data, rather than strongly supported by them. Nevertheless, our results demonstrate that an easy-to-measure genetic observable such as the mutation trajectory can greatly restrict the set of models that are consistent with a measured fitness trajectory. Additional information about the genetic diversity within the population (e.g., measured from pairwise heterozygosity among clones) will likely provide even more power to distinguish between competing hypotheses. The computational framework developed here provides a powerful and flexible method for incorporating this genetic information as it becomes available.

MATERIALS AND METHODS

Fitness trajectories. The fitnesses of the LTEE strains were calculated from Eq. (1) using the raw competition assays reported by Wiser et al. (2013). The quantity $f/(1-f)$ was estimated from the ratio of red and white colonies when plated on arabinose media, and the duration each competition was $\Delta t = \log_2(100) \approx 6.6$ generations. The fitness gains between generation 40,000 and 50,000 were calculated in a similar manner, but with a longer competition time of $\Delta t = 3 \log_2(100) \approx 19.9$ generations. Subsequent analysis of the fitness trajectory was restricted to the six non-mutator populations with complete fitness measurements: Ara-5, Ara-6, Ara+1, Ara+2, Ara+4, and Ara+5 (Wiser et al., 2013). Notably, this subset excludes both the citrate-metabolizing population (Ara-3) studied by Blount et al. (2008), as well as the crossfeeding population (Ara-2) studied by Plucain et al. (2014).

Fitness effects of individual mutations. The fitness effects of the five mutations in Fig. S6 were calculated from the raw competition assays reported by Khan et al. (2011). The fitness effect s was defined as the difference between the fitness of the mutant and background genotypes, which were estimated from the competition assays using the same procedure as above.

The mutation trajectory. The total number of genetic changes was estimated from the DNA sequences of clones analyzed by Barrick et al. (2009) and Wielgoss et al. (2011). The finalized mutation calls for the clones in Barrick et al. (2009) were obtained from supplementary tables 1 and 2 of that work, and the mutation calls for the clones in Wielgoss et al. (2011) were obtained from the supplementary data files available at http://barricklab.org/twiki/pub/Lab/SupplementLongTermMutationRates/long-term_mutation_rates.zip. To obtain a more densely sampled mutation trajectory, we included clones from populations that were excluded from the fitness trajectory analysis above. This includes seven clones sampled from the Ara-1 population prior to the spread of the mutator phenotype, and two clones sampled from the Ara-3 population prior to the spread of the citrate-metabolizing phenotype. The complete list of included clones is given in Table S1.

Population genetic simulations. Simulated fitness and mutation trajectories were obtained from a forward-time algorithm designed to mimic the serial transfer protocol of the LTEE. Between each transfer, lineages are assumed to expand clonally for $\log_2(100) \approx 6.64$ generations at a deterministic exponential growth rate $r = r_0 + X$, where X is the fitness relative to the ancestor. At the transfer step, the population is diluted 100-fold (with Poisson sampling noise) to $N_b = 5 \times 10^6$ individuals. Mutations accumulate at a constant rate U during the growth phase, but we assumed that they do not significantly influence the fitness of the individual until the next transfer cycle. Thus, mutation was approximated by assuming that each individual has a probability $6.64 \cdot U$ of gaining a mutation at the end of a transfer step, with additive fitness effects drawn from the genotype-specific DFE, $\rho(s|\vec{g})$. A copy of our implementation in C++ will be made available upon publication of this manuscript.

Likelihood estimation. The likelihood of each parameter combination was estimated from simulations using Eq. (4). To speed computation, we simulated 18 replicate populations and generated $n = 10,000$ different 6-population averages by bootstrap resampling. The scaled likelihood Λ [which differs from $p(\vec{X}_{\text{obs}}|\theta)$ by a constant

factor] was defined as

$$\Lambda \equiv \sum_{i=1}^n \prod_{\{t_k\}} \exp \left[-\frac{(\bar{X}_{\text{obs}}(t_k) - \bar{X}_i(t_k))^2}{2\sigma_{\text{err}}^2} \right], \quad (27)$$

where the measurement uncertainty $\sigma_{\text{err}} \approx 1.4\%$ was estimated from Fig. 1B.

Statistical tests. The consistency of each parameter combination was assessed using a χ^2 goodness-of-fit test. We simulated 18 replicate populations to estimate $\bar{X}(t)$, and we generated $n = 10,000$ different 6-population averages by bootstrap resampling these replicates and adding unbiased Gaussian measurement noise with $\sigma_{\text{err}} = 1.4\%$. The p -value is then approximated by

$$\Pr[\chi^2 > \chi_{\text{obs}}^2 | \theta] \approx \frac{1}{n} \sum_{i=1}^n \theta(\chi_i^2 - \chi_{\text{obs}}^2) \quad (28)$$

where $\theta(x)$ is the Heaviside step function and χ_i^2 is the mean squared error,

$$\chi_i^2 \equiv \sum_{t_k} (\bar{X}_i(t_k) - \bar{X}(t_k))^2. \quad (29)$$

The posterior predictive p -value for the entire model is then defined by

$$p = \frac{\int \Pr[\chi > \chi_{\text{obs}} | \theta] p(\bar{X}_{\text{obs}} | \theta) p(\theta) d\theta}{\int p(\bar{X}_{\text{obs}} | \theta) p(\theta) d\theta}, \quad (30)$$

where $p(\theta)$ is the prior distribution of parameter values.

ACKNOWLEDGMENTS

We thank Sergey Kryazhimskiy, Elizabeth Jerison, and Daniel Rice for useful discussions. This work was supported in part by a National Science Foundation Graduate Research Fellowship, the James S. McDonnell Foundation, the Alfred P. Sloan Foundation, the Harvard Milton Fund, grant PHY 1313638 from the NSF, and grant GM104239 from the NIH. Simulations in this paper were performed on the Odyssey cluster supported by the Research Computing Group at Harvard University.

REFERENCES

- E M Quandt, D E deatherage, A D Ellington, G Georgiou, and J E Barrick. Recursive genomewide recombination and sequencing reveals a key refinement step in the evolution of a metabolic innovation in *Escherichia coli*. *Proc Natl Acad Sci*, 111:2217–2222, 2014.
- D M Weinreich, N F Delaney, M A DePristo, and D L Hartl. Darwinian evolution can follow only very few mutational paths to fitter proteins. *Science*, 312:111–114, 2006.

- S Wright. The roles of mutation, inbreeding, crossbreeding and selection in evolution. In *Proceedings of the VI International Congress of Genetics*, pages 356–366, 1932.
- Stephen J Gould. *Wonderful life: the Burgess Shale and the nature of history*. W W Norton, New York, 1989.
- J. Arjan G.M. de Visser and Joachim Krug. Empirical fitness landscapes and the predictability of evolution. *Nature Reviews Genetics*, 15:480–490, 2014.
- D Segrè, A Deluna, GM Church, and R Kishony. Modular epistasis in yeast metabolism. *Nat Genet*, 37:77–83, 2005.
- Robert P St Onge, Ramamurthy Mani, Julia Oh, Michael Proctor, and *et al.* Systematic pathway analysis using high-resolution fitness profiling of combinatorial gene deletions. *Nature Genetics*, 39:199 – 206, 2007.
- Justin B Kinney, Anand Murugana, Curtis G Callan, Jr, and Edward C Cox. Using deep sequencing to characterize the biophysical mechanism of a transcriptional regulatory sequence. *Proc Natl Acad Sci*, 107:9158–9163, 2010.
- Michael Costanzo, Anastasia Baryshnikova, Jeremy Bellay, Yungil Kim, and *et al.* The genetic landscape of a cell. *Science*, 327:425–431, 2010.
- Lukasz Jasnos and Ryszard Korona. Epistatic buffering of fitness loss in yeast double deletion strains. *Nature Genetics*, 39:550–554, 2007.
- R A Fisher. The distribution of gene ratios for rare mutations. *Proc Roy Soc Edinburgh*, 50:204–219, 1930.
- J F C Kingman. A simple model for the balance between selection and mutation. *J Appl Prob*, 15:112, 1978.
- S Kauffman and S Levin. Towards a general theory of adaptive walks on rugged landscapes. *J Theor Biol*, 128:11–45, 1987.
- S Kauffman and E D Weinberger. The nk model of rugged fitness landscape and its application to maturation of the immune response. *J Theor Biol*, 141:211–245, 1989.
- O K Silander, O Tenaillon, and L Chao. Understanding the evolutionary fate of finite populations: The dynamics of mutational effects. *PLoS Biol*, 5:e94, 2007.
- R C MacLean, G G Perron, and A Gardner. Diminishing returns from beneficial mutations and pervasive epistasis shape the fitness landscape for rifampicin resistance in *Pseudomonas aeruginosa*. *Genetics*, 186:1345–1354, 2010.
- Craig R Miller, Paul Joyce, and Holly A Wichman. Mutational effects and population dynamics during viral adaptation challenge current models. *Genetics*, 187:185–202, 2011.
- Claudia Bank, Ryan T Hietpas, Alex Wong, Daniel N Bolon, and Jeffrey D Jensen. A bayesian mcmc approach to assess the complete distribution of fitness effects of new mutations: Uncovering the potential for adaptive walks in challenging environments. *Genetics*, 196:841–852, 2014.
- B H Good, I M Rouzine, D J Balick, O Hallatschek, and M M Desai. Distribution of fixed beneficial mutations and the rate of adaptation in asexual populations. *Proc. Natl. Acad. Sci.*, 109:4950–4955, 2012.
- C L Burch and L Chao. Evolvability of an rna virus is determined by its mutational neighbourhood. *Nature*, 406: 625–628, 2000.
- J E Barrick, M R Kauth, C C Strelhoff, and R E Lenski. *Escherichia coli* rpoB mutants have increased evolvability in proportion to their fitness defects. *Mol Biol Evol*, 27: 1338, 2010.
- Robert J Woods, Jeffrey E Barrick, Tim F Cooper, Utpala Shrestha, Mark R Kauth, and Richard E Lenski. Second-order selection for evolvability in a large *Escherichia coli* population. *Science*, 331:1433–1436, 2011.
- S K Kryazhimskiy, D P Rice, and M M Desai. Population subdivision and adaptation in asexual populations of *saccharomyces cerevisiae*. *Evolution*, 66:1931–1941, 2012.
- L Perfeito, A Sousa, T Bataillon, and I Gordo. Rates of fitness decline and rebound suggest pervasive epistasis. *Evolution*, 68:150–162, 2014.
- S K Kryazhimskiy, D P Rice, E R Jerison, and M M Desai. Global epistasis makes adaptation predictable despite sequence-level stochasticity. *Science*, 344:1519–1522, 2014.
- G I Lang, D P Rice, M J Hickman, E Sodergren, G M Weinstock, D Botstein, and M M Desai. Pervasive genetic hitchhiking and clonal interference in forty evolving yeast populations. *Nature*, 500:571–574, 2013.
- E M Frenkel, B H Good, and M M Desai. The fates of mutant lineages and the distribution of fitness effects of beneficial mutations in laboratory budding yeast populations. *Genetics*, 196:1217–1226, 2014.
- S A Frank. Generative models versus underlying symmetries to explain biological pattern. *Journal of Evolutionary Biology*, 27:1172–1178, 2014.
- M J Wiser, N Ribeck, and R E Lenski. Long-term dynamics of adaptation in asexual populations. *Science*, 342:1364–1367, 2013.
- S Kryazhimskiy, G Tkaik, and J B Plotkin. The dynamics of adaptation on correlated fitness landscapes. *Proc Natl Acad Sci USA*, 106:18638–18643, 2009.
- Richard E. Lenski, Michael R. Rose, Suzanne C. Simpson, and Scott C. Tadler. Long-term experimental evolution in *escherichia coli*. i. adaptation and divergence during 2,000 generations. *The American Naturalist*, 138:1315–1341, 1991.
- R E Lenski and M Travisano. Dynamics of adaptation and diversification: A 10,000-generation experiment with bacterial populations. *Proc Natl Acad Sci USA*, 91:6808–6814, 1994.
- P Sibani, M Brandt, and P Alstrøm. Evolution and extinction dynamics in rugged fitness landscapes. *Intl J Mod Phys*, 12: 361–391, 1998.
- Michael M. Desai and Daniel S. Fisher. Beneficial mutation selection balance and the effect of genetic linkage on positive selection. *Genetics*, 176:1759–1798, 2007.
- Jeffrey E Barrick, Dong Su Yu, Sung Ho Yoon, Haeyoung Jeong, and *et al.* Genome evolution and adaptation in a long-term experiment with *Escherichia coli*. *Nature*, 461: 1243–1247, 2009.
- S Wielgoss, J E Barrick, O Tenaillon, S Cruveiller, B Chane-Woon-Ming, C Médigue, R E Lenski, D Schneider, and B J Andrews. Mutation rate inferred from synonymous substitutions in a long-term evolution experiment with *escherichia coli*. *G3 (Bethesda)*, 1:183–186, 2011.
- Sbastien Wielgoss, Jeffrey E. Barrick, Olivier Tenaillon, Michael J. Wiser, and *et al.* Mutation rate dynamics in a bacterial population reflect tension between adaptation and genetic load. *Proc Natl Acad Sci*, 110:222227, 2013.
- Aisha I Khan, Duy M Din, Dominique Schneider, Richard E Lenski, and Tim F Cooper. Negative epistasis between beneficial mutations in an evolving bacterial population. *Science*, 332:1193–1196, 2011.
- P.J. Gerrish and R.E. Lenski. The fate of competing beneficial mutations in an asexual population. *Genetica*, 127:127–144, 1998.
- Olivier Tenaillon, Alejandra Rodriguez-Verdugo, Rebecca L Gaut, Pamela McDonald, Albert F Bennett, Anthony D

- Long, and Brandon S Gaut. The molecular diversity of adaptive convergence. *Science*, 335:457–461, 2012.
- J.B.S. Haldane. The mathematical theory of natural and artificial selection, part v: selection and mutation. *Proc. Camb. Philos. Soc.*, 23:828–844, 1927.
- J.H. Gillespie. Molecular evolution over the mutational landscape. *Evolution*, 38:1116–1129, 1984.
- H.A. Orr. The population genetics of adaptation: the adaptation of dna sequences. *Evolution*, 56:1317–1330, 2002.
- Hsin-Hung Chou, Hsuan-Chao Chiu, Nigel F. Delaney, Daniel Segr, , and Christopher J. Marx. Diminishing returns epistasis among beneficial mutations decelerates adaptation. *Science*, 332:1190–1192, 2011.
- Anna C Nagel, Paul Joyce, Holly A Wichman, and Craig R Miller. Stickbreaking: A novel fitness landscape model that harbors epistasis and is consistent with commonly observed patterns of adaptive evolution. *Genetics*, 190:655–667, 2012.
- H A Wichman, M R Badgett, L A Scott, C M Boulianne, and J J Bull. Different trajectories of parallel evolution during viral adaptation. *Science*, 285:422–424, 1999.
- J Draghi and J B Plotkin. Selection biases the prevalence and type of epistasis along adaptive trajectories. *Evolution*, 67:3120–3131, 2013.
- Zachary D Blount, Christina Z Borland, and Richard E Lenski. Historical contingency and the evolution of a key innovation in an experimental population of *Escherichia coli*. *Proc Natl Acad Sci*, 105:7899–7906, 2008.
- Jessica Plucoin, Thomas Hindré, Mickaël Le Gac, Olivier Tenaillon, and *et al.* Epistasis and allele specificity in the emergence of a stable polymorphism in *Escherichia coli*. *Science*, 343:1366–1369, 2014.

SUPPLEMENTAL INFORMATION

Generation	Clone ID	Population	Source
2,000	REL1164A	Ara-1	Barrick et al. (2009)
5,000	REL2179A	Ara-1	Barrick et al. (2009)
10,000	REL4536A	Ara-1	Barrick et al. (2009)
15,000	REL7177A	Ara-1	Barrick et al. (2009)
20,000	REL8593A	Ara-1	Barrick et al. (2009)
	REL8593A, REL8593B, REL8593C	Ara-1	Wielgoss et al. (2011)
30,000	ZDB16, ZDB357	Ara-3	Wielgoss et al. (2011)
40,000	REL10947, REL10948, REL10949	Ara-5	Wielgoss et al. (2011)
	REL11005, REL11006	Ara-6	Wielgoss et al. (2011)
	REL11008, REL11009	Ara+1	Wielgoss et al. (2011)
	REL10950, REL10951	Ara+2	Wielgoss et al. (2011)
	REL10956, REL10957	Ara+4	Wielgoss et al. (2011)
	REL10982, REL10983	Ara+5	Wielgoss et al. (2011)

TABLE S1 A list of the clones used to estimate the mutation trajectory in Fig. 1B.

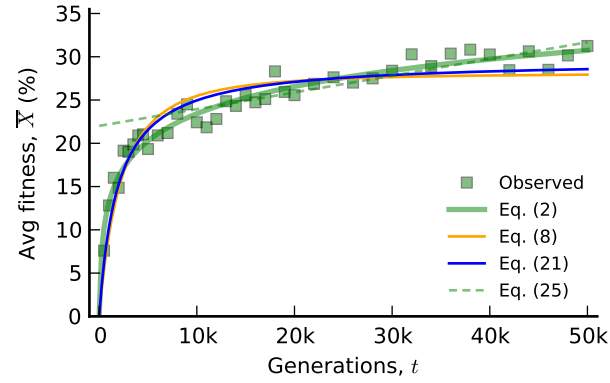


FIG. S1 Comparison of the four analytical fitness trajectories in Eqs (2), (8), (21), and (25). The best-fit parameters were obtained by minimizing the mean squared error, and the fit of the linear trajectory in Eq. (25) was restricted to the last 40,000 generations of evolution.

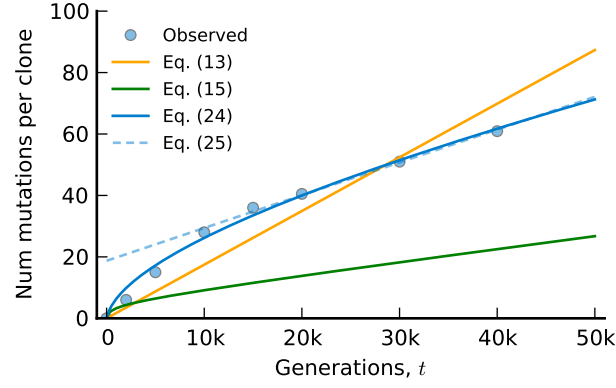


FIG. S2 Comparison of the four analytical mutation trajectories in Eqs (13), (15), (24), and (25). The best-fit parameters were obtained by minimizing the mean squared error in the presence of an unknown neutral mutation rate $0 \leq U_n \leq U_{\text{tot}}$, and the fit of the linear trajectory in Eq. (25) was restricted to the last 40,000 generations of evolution.

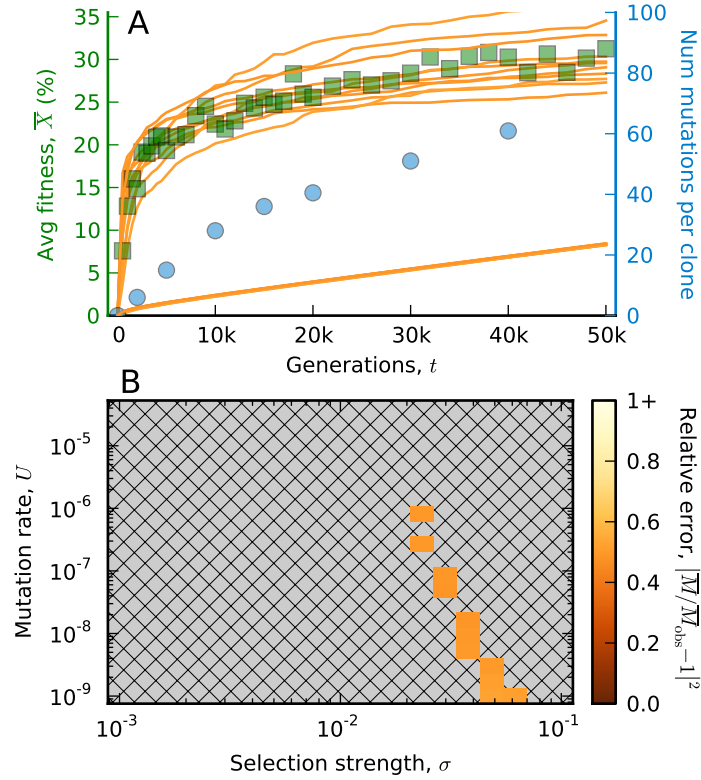


FIG. S3 Fitting an uncorrelated landscape model to the LTEE data. An analogous version of Fig. 2 constructed for the uncorrelated landscape model in Eq. (14) with an exponential ancestral DFE. Note the change in scale for the relative error in the mutation trajectory. To ensure better convergence of the ensemble mean fitness trajectory, we simulated 100 independent populations for bootstrap resampling instead of the 18 used for the other models.

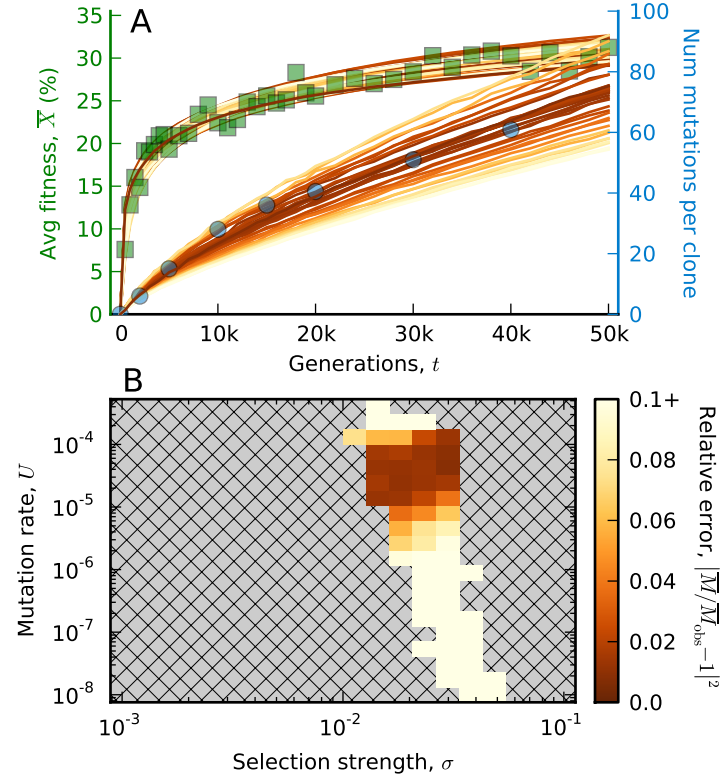


FIG. S4 An analogous version of Fig. 3 for a truncated exponential ancestral DFE ($s_{\max} = 4\sigma$).

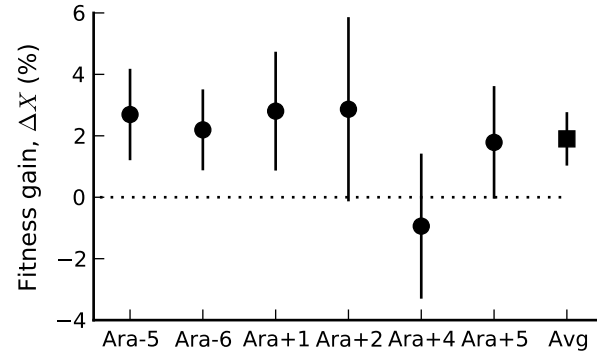


FIG. S5 The change in fitness between generation 40,000 and 50,000 for the six non-mutator populations in Fig. 1A, estimated from the non-ancestral competition assays in Wiser et al. (2013) (see Methods). Error bars denote 2 stderr confidence intervals.

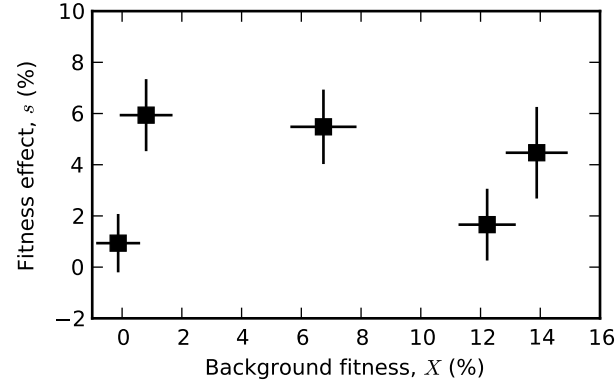


FIG. S6 The fitness effects (along the line of descent) for the first 5 mutations to fix in the Ara-1 population, estimated from the genetic reconstruction data of Khan et al. (2011) (see Methods). On the x -axis, each mutation is plotted according to the fitness of the genetic background in which it arose. Error bars denote 2 stderr confidence intervals.

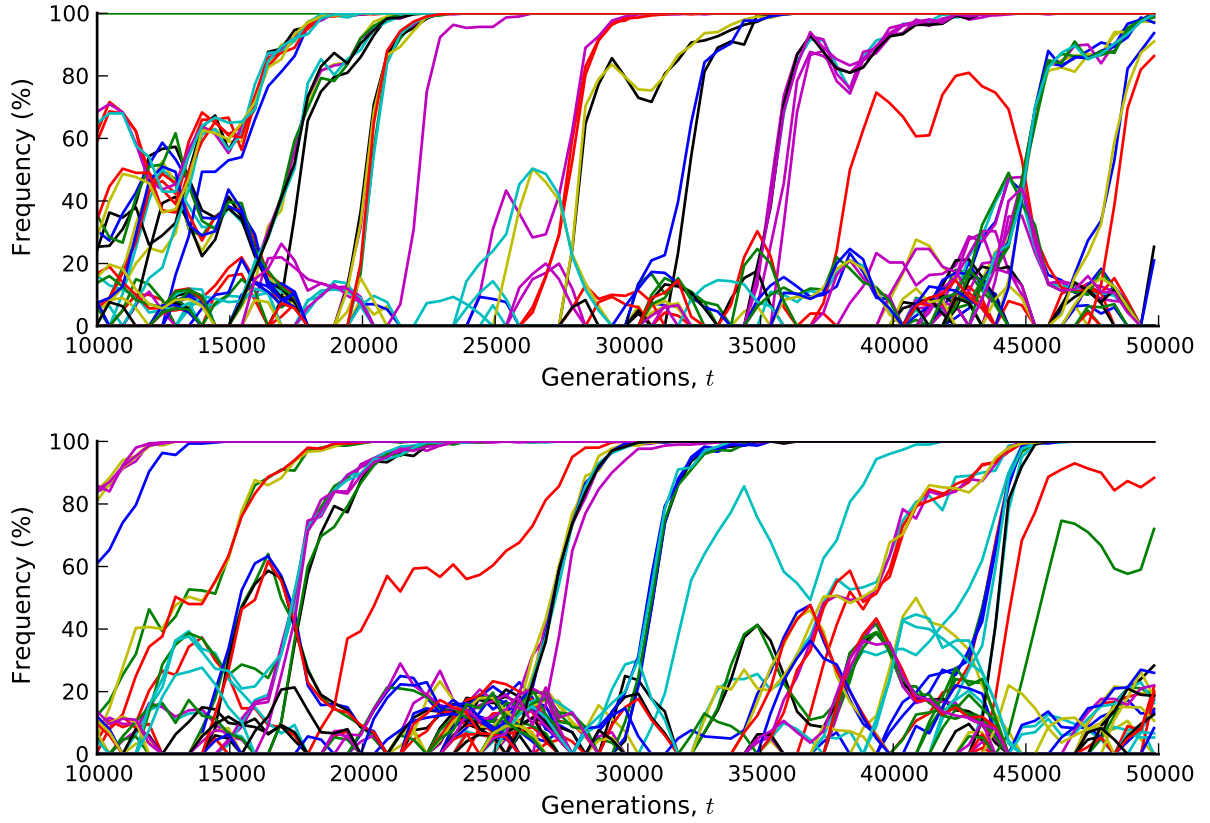


FIG. S7 Simulated mutational dynamics for the constant truncated exponential DFE in Fig. 4. Colored lines depict the frequencies of all mutations that rose above 5% in the first 50,000 generations. To mimic whole-population sequencing in the LTEE, mutation frequencies are sampled in 500 generation intervals with binomial sampling noise ($n = 300$). Parameter values are $U = 2.6 \times 10^{-6}$, $\sigma = 1.1 \times 10^{-3}$, and $U_n = 4 \times 10^{-4}$ (top) and $U = 2.5 \times 10^{-5}$, $\sigma = 7 \times 10^{-4}$, and $U_n = 1.3 \times 10^{-4}$ (bottom).